Geomechanics and Engineering, *Vol. 28, No. 2 (2022) 181-195*
https://doi.org/10.12989/gae.2022.28.2.181

An experimental study on triaxial failure mechanical behavior of jointed specimens with different JRC

Wen-Ling Tian[1], Sheng-Qi Yang*[1], Jin-Peng Dong[1], Jian-Long Cheng[2] and Jia-wei Lu[1]

[1]*State Key Laboratory for Geomechanics and Deep Underground Engineering, School of Mechanics and Civil Engineering, China University of Mining and Technology, Xuzhou 221116, P.R. China*
[2]*State Key Laboratory of Geohazard Prevention and Geoenvironment Protection, Chengdu University of Technology, Chengdu 610059, China*

(Received May 12, 2021, Revised October 14, 2021, Accepted October 23, 2021)

Abstract. Roughness and joint inclination angle are the important factors that affect the strength and deformation characteristics of jointed rock mass. In this paper, 3D printer has been employed to make molds firstly, and casting the jointed specimens with different joint roughness coefficient (*JRC*), and different joint inclination angle (α). Conventional triaxial compression tests were carried out on the jointed specimens, and the influence of *JRC* on the strength and deformation parameters was analyzed. At the same time, acoustic emission (AE) testing system has been adopted to reveal the AE characteristic of the jointed specimens in the process of triaxial compression. Finally, the morphological of the joint surface was observed by digital three-dimensional video microscopy system, and the relationship between the peak strength and *JRC* under different confining pressures has been discussed. The results indicate that the existence of joint results in a significant reduction in the strength of the joint specimen, *JRC* also has great influence on the morphology, quantity and spatial distribution characteristics of cracks. With the increase of *JRC*, the triaxial compressive strength increase, and the specimen will change from brittle failure to ductile failure.

Keywords: joint inclination angle; joint roughness coefficient; morphology; rock mechanics; triaxial compression

1. Introduction

As we all know, engineers often subjected to substantial problems related to jointed rock masses in mining, municipal, oil exploration projects and so on (Lee *et al*. 2020). The development of joints often brings hidden dangers to some projects such as dams, slopes and underground caverns, and leads to instability and destruction of engineering rock masses (Mamen and Hammoud 2021). The joints, which are regarded as a significant structural plane, are widely distributed inside the rocks. The stability of jointed rock masses is not only related to the strength of intact rocks, but also controlled by the joint surface. Therefore, it is very essential to research the mechanical behavior of jointed specimens.

The study on the strength of intact and fissured rocks has been very exhaustive and in-depth (Yang *et al*. 2017, Diamantis 2019, Cai *et al*. 2021), and the mechanical properties of the joint planes are the key factors in the evaluation of rock mass stability. The sawtooth joint surface is widely observed in the slope and excavation engineering, so the research on the strength of jointed rock mass not only has theoretical significance, but also directly guides the reinforcement and design of related rock mass engineering (Samanta *et al.* 2018). Simultaneously, the existence of joints has a vital influence on the mechanical properties of rock. Therefore, the mechanics parameters of jointed rock are also important factors that must be considered when analyzing, evaluating and designing actual rock engineering (Abolfazli and Fahimifarb, 2020).

The earliest research on the roughness of the joint surface is derived from the strength criterion summarized by Patton (1966) for the rock mass structural plane with regular sawtooth.

$$\tau = \sigma_n \tan(\varphi + i) \tag{1}$$

where φ is the friction angle of the joint plane, σ_n is normal stress and i is the undulation angle of the convex of the structural plane. However, the induction of this equation is derived in a special case. In reality, rock joint surfaces cannot be regular straight or sawtooth shapes, and in most cases are rugged and irregular. Barton (1973), who proposed a new empirical equation based on the study of the shear strength of joint surfaces performed by Patton, uses the *JRC*, which can be determined by comparison method or inverse calculation based on direct shear test, to describe the topography of the rough surface. The Barton criterion become the most widely used strength criterion as a result of its simple form and ability to reflect the roughness of irregular joint surfaces. Barton and Choubey (1977) then proposed 10 standard contour curves to describe the 10 rough structural surface morphology levels with *JRC* range 0-20. And, this method has been promoted by ISRM. In the theoretical research stage, many scholars have established the correlation criterion between roughness

*Corresponding author, Professor
E-mail: yangsqi@hotmail.com

ISSN: 2005-307X (Print), 2092-6219 (Online)

parameter or fractal dimension (D) and structural surface roughness coefficient through the regression analysis between roughness parameters of the standard contour curve as well as the fractal dimension and *JRC*. And these equations can be used to estimate *JRC* (Xie *et al*. 1998, Marsch and Fernandez-Steeger 2021).

With the support of theoretical research on rough jointed rock, scholars have acquired remarkable achievements in experimental research and numerical simulation of rough jointed rocks (Yang *et al.* 2020). The experimental researches on rough jointed rocks mainly focus on shear and permeability tests. Zandarin *et al.* (2013) have carried out shear tests on saw-toothed jointed rock with different undulation angles and performed numerical simulation to study the influence of joint roughness and suction on its strength. Grasselli *et al.* (2002, 2003, 2006) established a statistical function relationship between the effective shear dip angle of the joint surface micro-element and its corresponding contact area and proposed the three-dimensional topographic function of the joint surface by observing a large number of direct shear test of jointed rock. Jafari *et al.* (2003) performed repeated cyclic shearing on two kinds of artificial joints and simulated the shearing ability of joints under strong and weak earthquakes. Meanwhile, with respect to this kind of artificial joint, an intensity model considering shear rate, normal stress and cycle number is proposed as well. Singh and Basu (2016) explored the shear behaviors of real natural un-matching joints in granite, and most of the obtained behavioral patterns look different from the typical shear stress-shear displacement graph in the literature that are based on direct shear test results in case of matching rock discontinuities. Wang *et al*. (2019) conducted the iso-stress cyclic relaxation tests and shear stress relaxation stress on artificial rock discontinuity samples and natural rock discontinuity samples to investigate the stress relaxation behavior and the influence of stress history and surface morphology. Zhao *et al.* (2019) conducted direct shear tests on a series of thermally-treated granite specimens including a rough fracture, and the result shows that thermally-induced microcracks are the main source of the change in fracture shear properties. Renaud *et al.* (2019) suggest that only little degradation occurs along the contact specimens during the shear tests. He *et al.* (2020) and Hojat *et al.* (2021) proposed a piecewise function to calculate mobilized *JRC*, and discussed the variation in the friction angle at various stages. Ban *et al*. (2021) studied the contribution of the asperities with different apparent dip angles to shear strength, and then derived the shear strength of the entire joint asperities.

The above experimental studies are based on real rock mass specimens, but the experiment is not reproducible, and it is impossible to study the variation of mechanical properties of the same specimen under different conditions. Regarding the difficulty in determining *JRC*, the numerical simulation software is capable of simulating the joint surface and analyzing the mesoscopic characteristics of the joint surface and its failure mechanism more realistically. Xia *et al*. (2012) generated rough joint profiles and simulated its shear properties in a two-dimensional particle flow code (PFC^{2D}) and observed the macroscopic failure process of joints under direct shear test from a microscopic perspective. Park and Song (2013) used a bonded particle bonded model to conduct a direct shear test on rock joint, and it indicates that the joint roughness should be qualified with respect to the shear direction and the corresponding contact area. Bahaaddini (2016) experimentally and numerically studied the effect of boundary condition on the results of direct shear tests and revealed that the gap zone size has a significant effect on the shear mechanism. Saadat and Taheri (2020) proposed a cohesive grain based model to assess the effect of *JRC* on asperity damage and shear mechanism of jointed rock under constant normal load and constant normal stiffness conditions.

The above researches involve the shear and seepage tests of roughness jointed rocks, but the research results on triaxial compression experiments of roughness jointed rocks, which is capable of reflecting engineering problems, are relatively less (Guo and Qi 2015). Simultaneously, natural jointed specimens are difficult to core and the surface roughness is difficult to define. However, the rock-like material specimen can overcome this problem to some extent. The application of 3D printing technology can effectively solve the problem of non-repeatable test of rock mass's structural surface. Therefore, a group of rock-like materials were manufactured and their roughness joint were prefabricated first, then the GCTS RTX-4000 rock testing system was used to carry out the triaxial compression tests under different confining pressures. According to the test results, the influence of *JRC*, joint angle and confining pressure on the strength and failure characteristics of specimens was analyzed, which can provides guidance and suggestions for engineering construction of jointed rock masses.

2. Experimental material and loading procedure

2.1 Specimen preparation and material properties

According to the traditional Koch curve of Xie (1998), we established a theoretical fractal model of the joint profile to simulate the roughness of the joint profile. Based on this model, the fractal dimension D of the joint can be estimated directly from the two statistical parameters L and h (L and h are the average base length and average height of the joint roughness, respectively), which is given by

$$D=\log 4/\log\{2[1+\cos(\arctan(2h/L))]\} \tag{2}$$

$$JRC=85.2671(D-1)^{0.5679} \tag{3}$$

In this experiment, joint dip angle (α) set as 0°, 30°, 60°, 90°, and *JRC* set as 2, 12, 22 respectively, and the average base length (L) of the joint roughness is 5 mm, whose average height h is 0.22, 1.10, 2.00 mm, respectively. The design drawing of the joint surface curve of different *JRC* values is shown in Fig. 1(a). According to the designed joint surface curve in Fig. 1(a), and the 3D print *JRC* mold is shown in Fig. 1(b) and Fig. 1(c). The material used in mold is ABS, which is acrylonitrile-butadiene-styrene plastic. The

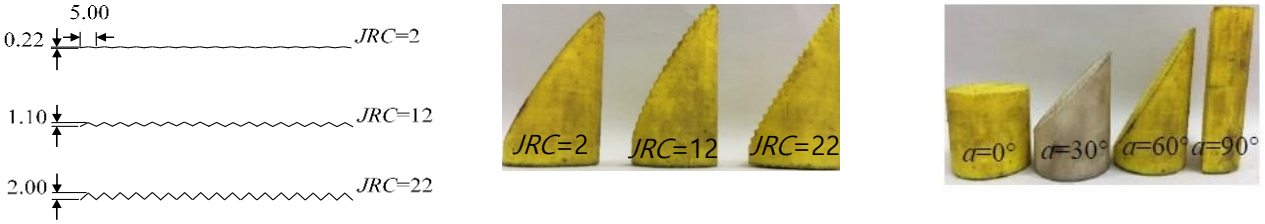

(a) Joint surface curve (b) Mold with different *JRC* (c) Mold with different angle

Fig. 1 Graph of *JRC* mold preparation

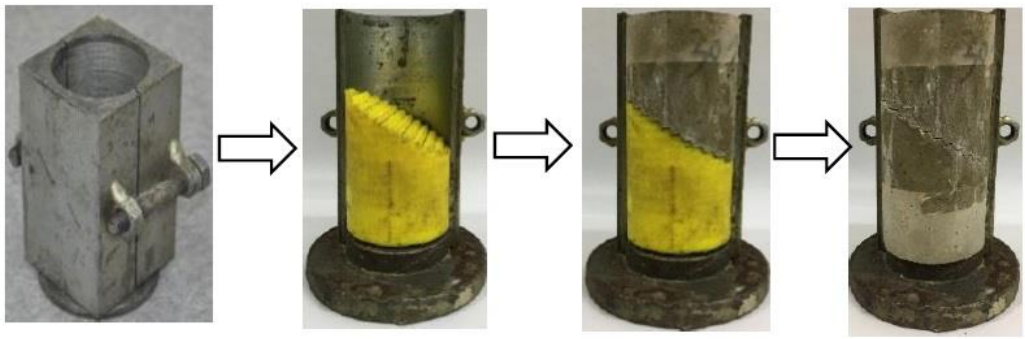

(a) steel mold (b) 3D mold is placed in the steel mold (c) pre-made half of the specimen (d) complete joint specimen

Fig. 2 Preparation of joint rock-like specimens (Yang *et al*. 2018)

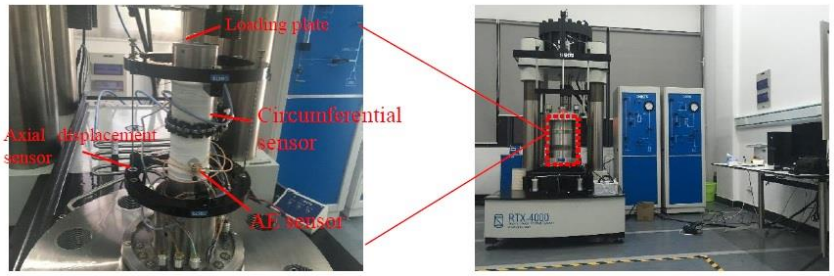

Fig. 3 GCTS RTX-4000 triaxial rock testing system

print size of the 3D printer is 200 mm × 200 mm × 185 mm, and the thickness of the printed layer of the mold is 0.14 mm. And also, the strength and precision of the printed mold all meet the test requirements.

The specimen preparation steps are:

1) The 3D printed mold is placed in the steel mold, as shown in Fig. 2(b). Subsequently, brush oil to the joint surface of the 3D printed mold to avoid breaking the joint surface during the disassembly process.

2) To add concrete paste into the steel mold. After waiting for about 24 hours, the mold was disassembled and the specimen is shown in Fig. 2(c) was obtained. Then, the specimen and the 3D printed mold were separated.

3) Place the pre-made half of the specimen into the mold, and then apply oil to the joint surface of the specimen again. Subsequently, repeat the above process to obtain a complete joint specimen.

4) After the specimen is cured for 28 days, the end faces of the specimen are polished to obtain a standard cylindrical specimen of 50 mm × 100 mm.

2.2 Test equipment and loading program

Conventional triaxial compression was carried out on the roughness jointed specimens by using the GCTS RTX–4000 high-pressure and high-temperature triaxial rock testing system, as shown in Fig. 3. The maximum axial loading capacity is 4000 kN, the maximum confining pressure is 140 MPa, and the maximum pore pressure is 140 MPa. The axial and circumferential deformation values were measured using axial and lateral linear variable differential transducers (LVDTs) with a range of ±2.5 mm.

The conventional triaxial experiments were carried out under different confining pressure of 5, 10, 15 and 20 MPa and it consist of the following two steps: First, the confining pressure was increased to the desired value at a constant rate of 4.0 MPa/min to ensure that the specimen was under uniform hydrostatic stresses. The deviatoric stress (σ_1 - σ_3) was then applied to the specimen at a loading rate of approximately 6.67×10^{-6}/s until the stage of post-peak failure. In the loading process, the axial strain can be

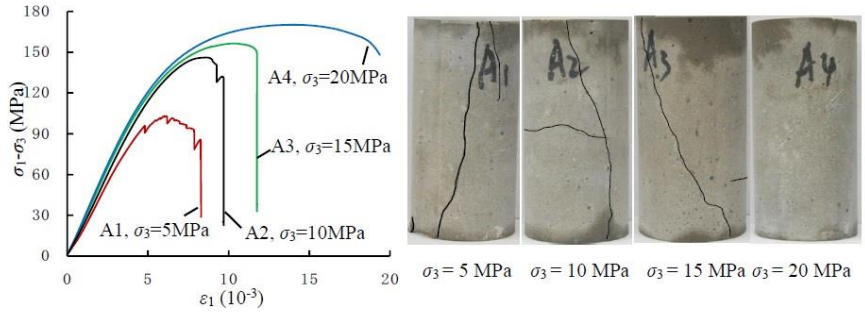

Fig. 4 Triaxial stress-strain curves and ultimate failure modes of intact rock-like specimens (Yang *et al*. 2018)

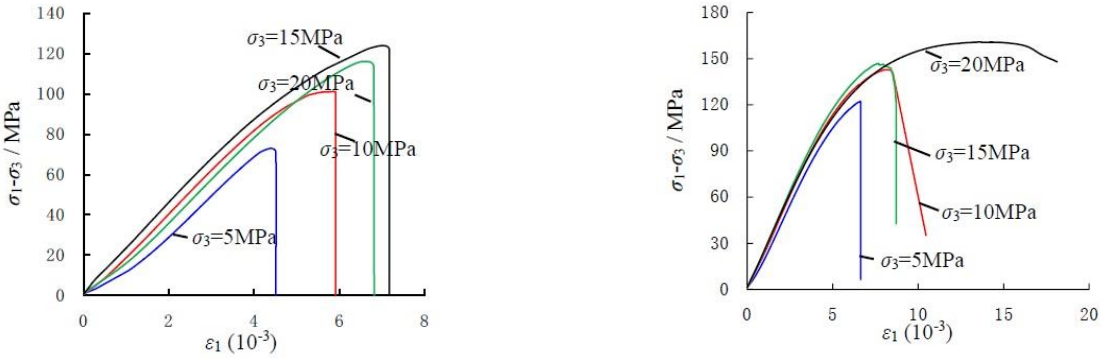

(a) α =60°, *JRC* = 12 (b) α =90°, *JRC* = 22

Fig. 5 The stress-strain curves of jointed specimens under triaxial compression

measured by two axial displacement sensors, and the one circumferential displacement sensor, as shown in Fig. 3. At the same time, during experimentation, the AE signal was monitored by using a micro-II AE measuring system made by PAC (Physical Acoustic Corporation).

3. Strength and deformation behavior of jointed specimens

Fig. 4 depicts the stress-strain curves of intact rock-like specimens under different confining pressures. It can be seen that the peak strength and peak strain of the intact specimen gradually increase with the increase of confining pressure, and that the specimen strength is in accordance with the Coulomb criteria. The peak strain of specimens under the effect of confining pressure increased by 16.9%, 18.6% and 64.7%, respectively. And from which we can see that the peak strain increases too much when the confining pressure increases from 15 MPa to 20 MPa, and the specimen changes from brittle failure to ductile failure.

Fig. 4 also shows the final fracture mode of intact specimens under triaxial compression with different confining pressure. At σ_3 = 5 MPa, specimen presents two axial tensile cracks, one of which is continuously extended from the bottom and across the whole specimen, while the other is initiated from the upper part. At σ_3 = 10 MPa, there are two cracks that initiate from the top and bottom respectively, and these two cracks meet at the middle of the specimen. Furthermore, a horizontal crack appears, probably because the horizontal force that occur when the failure surfaces slip each other. Nevertheless, the specimen belongs to axial tensile failure as a whole. When σ_3 = 15 MPa, the specimen has two shear rupture surfaces that meet together and form Y-type failure. As the confining pressure increases, the failure modes of the specimen tend to be simple. For example, there is no obvious crack on the surface of the specimen under σ_3 = 20 MPa, which can be explained by the fact that the confining pressure can closed the micro-cracks and pores inside the specimen and inhibit the crack slip. At the same time, the friction bearing capacity is improved after the micro-cracks and the pores are closed, making the axial deformation resistance.

Fig. 5 presents the stress-strain curves of jointed specimens under triaxial compression with α = 60°, *JRC* = 12 and α = 90°, *JRC* = 22, respectively. It is easy to see that the confining pressure has a great influence on the stress-strain curve. As the confining pressure increases, the compaction phase becomes shorter and the peak pre-yield stage becomes more apparently. Namely, there is significant plastic deformation before the peak strength. When α = 60°, *JRC* = 12, confining pressure has slight effect on the failure characteristic, and the specimens show brittle failure after the peak strength, as shown in Fig. 5(a). However, the specimens transfer from brittle to ductility failure with increasing of confining pressure when α = 90°, *JRC* = 22, as shown in Fig. 5(b). It means that confining pressure and α affects not only the peak strength of the specimen, but also its failure mode.

Fig. 6 illustrates the stress-strain curves of the jointed

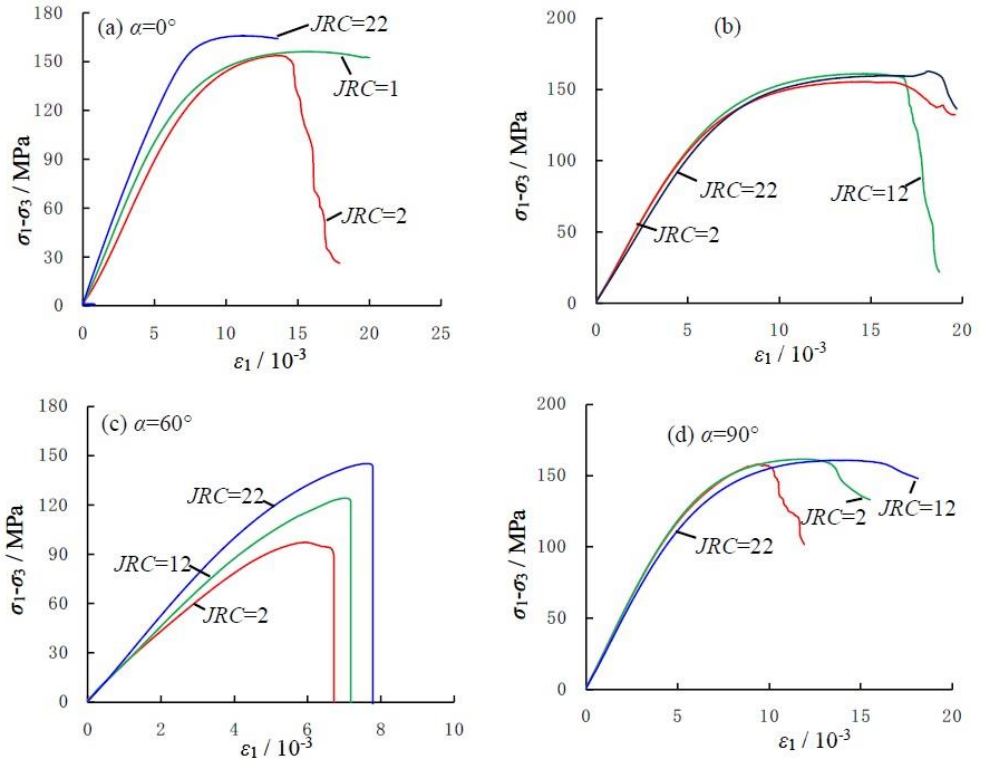

Fig. 6 Triaxial experiment Stress-strain curve of jointed specimens with different α and *JRC* under same confining pressure

specimens with α = 0°, 30°, 60° and 90° under triaxial compression (σ_3 = 20 MPa), it can be seen that *JRC* has different effect on the stress-strain curve of jointed specimens with different α. When α = 0° and 90°, stress-strain curve become more ductility after the peak strength with increasing *JRC*. However, the stress-strain curves of the jointed specimen with different *JRC* near coincide with each other when α = 30°. When α = 60°, it can be seen that *JRC* has a significant effect on the stress-strain curves, the peak strength increases with increasing *JRC*, whereas the specimens show brittle failure characteristic regardless of *JRC*.

Fig. 7 illustrates the peak strength of specimens of *JRC* = 2, 12, 22 at different α under σ_3 = 10 MPa. It can be seen that α has a certain influence on the peak strength. Namely, the peak strength of the specimen decreases first and then increases with the increase of the joint inclination angle. When α = 60°, the peak strength of the specimen is at the lowest value. When α = 0°, the peak strengths corresponding to the three *JRC* are 156.1 MPa, 156.6 MPa, 156.4 MPa respectively, and the average value is 156.4 MPa, which indicates that the peak strength is near constants. When α = 90°, the peak strengths corresponding to the three *JRC* are 158.1 MPa, 148.1 MPa, and 152.9 MPa, respectively, whose average value is 153 MPa and discrete coefficients is 6.53%. The peak strength of the intact specimen under σ_3 = 10 MPa is 156.2 MPa and it is very close to the peak strength of jointed specimens with α = 0 and 90°, which manifests that *JRC* has little effect on the strength of specimens when α = 0° and 90°.

The peak strength of joint specimens increases near linearly with the confining pressure, which can be fitted by

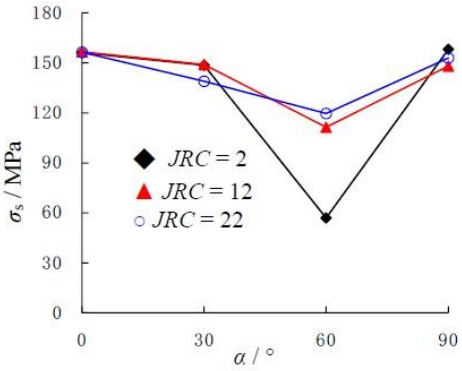

Fig. 7 Effect of α on the peak strength of joint specimen under triaxial compression (σ_3 = 10 MPa)

the linear Mohr-Coulomb criterion, i.e., Eq. (4).

$$\sigma_s = \sigma_c + q\sigma_3 = \frac{2C\cos\varphi + \sigma_3(1+\sin\varphi)}{1-\sin\varphi} \tag{4}$$

where σ_s is the maximum supporting capacity and σ_c and q are related to the cohesion C and the internal friction angle φ of rock.

According to the Mohr-Coulomb criterion, the linear correlation coefficient R^2 range from 0.90 to 1.00, which indicates that the peak strength of jointed specimens has a good positive linear correlation with the confining pressure. It can be seen from the slope q that the sensitivity of the intact and jointed specimens to the confining pressure is different. The peak strength of intact specimens has the most sensitivity to confining pressure, while the jointed specimens have different sensitivities due to different α and

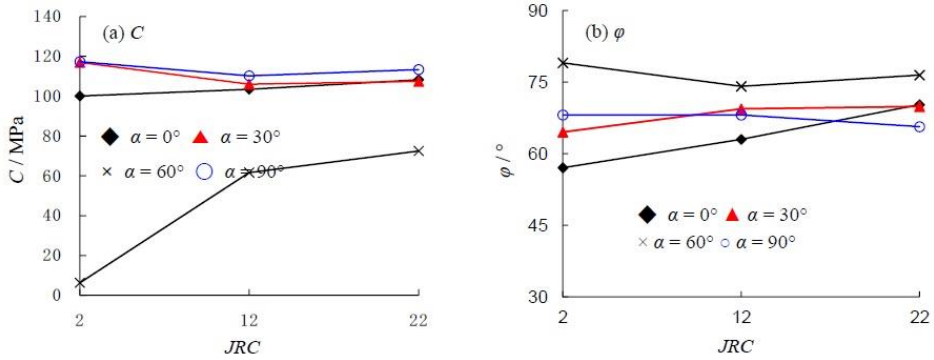

Fig. 8 Effect of *JRC* on cohesion and the internal friction angle of rock-like specimen

JRC. The specimen with α = 60° is relatively sensitive to confining pressure, and the average value of slope q is above 4.00; the specimen with α = 0° has the least sensitivity to confining pressure and the average value of slope q is the lowest as well.

The Mohr-Coulomb criterion is one of the most widely used strength theories in geotechnical engineering. According to Mohr-Coulomb criterion, the cohesion and internal friction angle can be easily obtained. As shown in Fig. 8(a), C of the specimen with α = 60° is smaller than that of other α. Moreover, C of the jointed specimens with α = 0° and α = 60° increases with the increase of *JRC*. However, C of the jointed specimens with α =30° and 90° decreases first and then increases, and it has the minimum value at *JRC* = 12. In addition, when α = 60°, *JRC* has a significant influence on C compared to the other α. However, it can be seen from the Fig. 8(b) that the *JRC* has only a slight influence on φ of the jointed specimens, the change of which is different from that of C. On the whole, φ of the jointed specimens with α = 0° and 30° increases with the increase of *JRC*; while φ of the jointed specimens with α = 60° decreases first and then increases, and φ of the jointed specimen with α = 90° decreases gradually.

4. Analysis of AE and damage characteristics

The jointed rock was analyzed in this paper from stress-strain curve, strength, deformation parameters, but not from its failure mechanism and failure process. In this section, the jointed rock will be analyzed from its failure characteristics, and the main conclusion is that the specimens are mainly shear failure under triaxial compression except for a small amount of axial splitting failure.

4.1 Analysis of failure mode

Fig. 9 shows the ultimate failure modes of triaxial compression of different *JRC* and α under triaxial compression. According to the triaxial compression test results of jointed specimens, there are three typical failure modes of jointed specimens with different *JRC*: I) Axial splitting failure: the mechanism resulting in such mode is the tensile failure of the specimen, forming a tensile crack parallel to the direction of the axial stress; II) Shear slip failure: the dilatancy shear failure appear in the specimen, and the failure surface is relatively complicated; III) Mixture shear and splitting failure: the tensile crack formed during the shear slip process.

It can be obviously seen from the Fig. 9 that confining pressure, *JRC* and α all have a significant influence on the number, shape and distribution characteristics of cracks. The failure mode of the specimens with α = 0° and 90° is mainly axial splitting tensile, and there are also a few oblique shear failures, and *JRC* has a slight effect on the failure modes. It can be seen that there are multiply splitting tensile crack in the jointed when σ_3 = 20 MPa. The failure mode of the specimens with α = 60° are the shear slip failure along the joint plane. And when *JRC* is increased to 22 and the confining pressure is 15 MPa and 20 MPa, the specimen is mixture failure of tension and shear, which manifests that the effects of joint inclination, confining pressure and *JRC* are interactive. The evolution of failure modes of α = 60° with confining pressure and *JRC* is similar to that obtained by Guo and Qi (2015).

When α = 30° and the *JRC* value is relatively small, the shear strength of the joint plane is fairly low, so the failure mode of the specimen is shear failure. And also, the crack is generated at the end of the joint plane, and propagates and penetrates along the direction of the joint inclination, causing slip and shear failure of the specimen. However, when α = 30° and *JRC* = 22, with the increase of the axial load, the axial load has exceeded the compressive strength of the material before the shear crack generated at the joint surface. Therefore, only the axial splitting failure rather than the shear failure will happen in the specimen.

At the same time, the axial splitting failure of the specimen with α = 30° is different from that with α = 0° and 90°. When α = 0° and 90° cracks initiated from the end of the specimens, and the cracks gradually propagate until cutting the joint surface and extending to the other end. By contrast, the axial splitting cracks tend to propagate downwards from the joint surface when α = 30°. In addition, with the increase of *JRC*, the cracks will occur at the end of the joint surface, and will further propagate along the direction of axial loading when propagating to a certain extent.

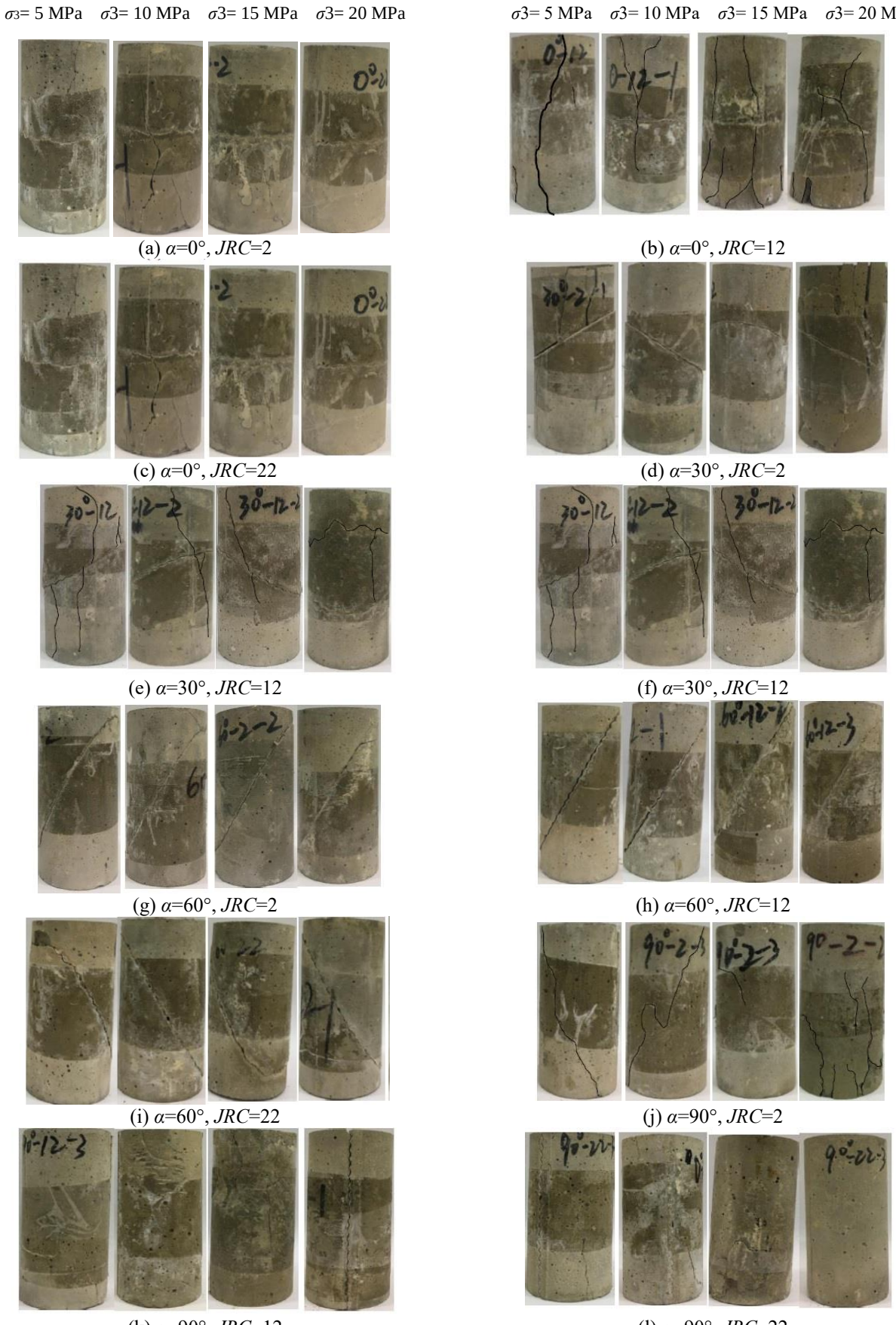

(a) α=0°, *JRC*=2 (b) α=0°, *JRC*=12

(c) α=0°, *JRC*=22 (d) α=30°, *JRC*=2

(e) α=30°, *JRC*=12 (f) α=30°, *JRC*=12

(g) α=60°, *JRC*=2 (h) α=60°, *JRC*=12

(i) α=60°, *JRC*=22 (j) α=90°, *JRC*=2

(k) α=90°, *JRC*=12 (l) α=90°, *JRC*=22

Fig. 9 Triaxial compression damage graph of rock samples including joint roughness

(a) *JRC* = 2 (b) *JRC* = 12 (c) *JRC* = 22

Fig. 10 Diagram of the joint surface failure of the specimen with $\alpha = 0°$

Table 1 Classification table of damage types of jointed rock-like specimens

σ_3 / MPa *α-JRC*	5	10	15	20
0°-2	I	I	I	I
0°-12	I	I	I	I
0°-22	I	I	I	I
30°-2	III	III	III	III
30°-12	III	III	III	III
30°-22	I	I	I	I
60°-2	II	II	II	II
60°-12	II	II	II	II
60°-22	II	II	III	III
90°-2	II	II	I	I
90°-12	I	I	I	I
90°-22	I	I	I	I

Note: I represents the axial splitting tensile failure; II represents the shear failure; III represents mixed tensile and shear failure

To compare the crack types more intuitively, the failure modes of the specimens are summarized in the Table 1. It can be found from the Table 1 that the failure modes of intact specimens under four confining pressures are all axial splitting failure, but when the specimen has joints, the influence of confining pressure, α and *JRC* on the failure mode of the specimen is complicated. As shown in the Table 1, when $\alpha = 0°$, the failure mode of the specimen is mainly axial splitting failure, but we cannot judge the influences of joint surface roughness on the failure mode of rock. However, the joint surface failure modes of *JRC* = 2, 12, 22 under σ_3 = 10 MPa for a specimen with $\alpha = 0°$ (as shown in Fig. 10 indicates that the number of axial splitting cracks cutting through the joint surface significantly increases with the increase of *JRC*. At *JRC* = 22, the failure of the joint surface is very complicated, and there are several cracks converging and then cutting the joint surface. This indicates that the failure mode of the specimen is mainly axial splitting failure when $\alpha = 0°$, whereas *JRC* has an effect on the failure of the jointed rock to some extent.

When $\alpha = 30°$, the axial load can generate shear stress at the joint surface, which is similar to the rock direct shear test where the joint surface is subjected to both normal and shear stresses. In this situation, when *JRC* = 2 and 12, the joint surface roughness is so low that the shear strength of the joint surface is relatively low. Therefore, shear failure and axial splitting failure occur in the specimen at the same time. However, the shear strength of the joint surface is increased when *JRC* = 22, and the axial load has reached the compressive strength of the specimen before the shear stress reaches the strength. Therefore, the specimen has only axial splitting failure. When $\alpha = 60°$, the shear stress generated by the axial load on the joint surface is significantly larger than that when $\alpha = 30°$, and the specimen belongs to the shear slip failure. When *JRC* = 22 and σ_3 = 15 and 20 MPa, the peak strength of the specimen also reaches the compressive strength, so there will be mixture failure of tension-shear. When $\alpha = 90°$, the failure modes of the specimen are mainly axial splitting failure.

4.2 Characteristics analysis of AE

Fig. 11 shows the stress-strain curve, AE counts and Accumulate AE counts of the jointed specimens under triaxial compression. In the initial stage, the stress-time curve is slightly concave, the stress rate is gradually increased, and there are different levels of AE events with higher ringing counts at this stage, which due to the close of the original cracks. With the increase of the axial stress, the specimen enters the elastic stage. In this stage, the axial stress is insufficient to form the micro-cracks. However, the saw-tooth on joint surface and some closed cracks inside them will also slip, so there are more ringing counts in each AE events, but the AE activity is still relatively less. As the

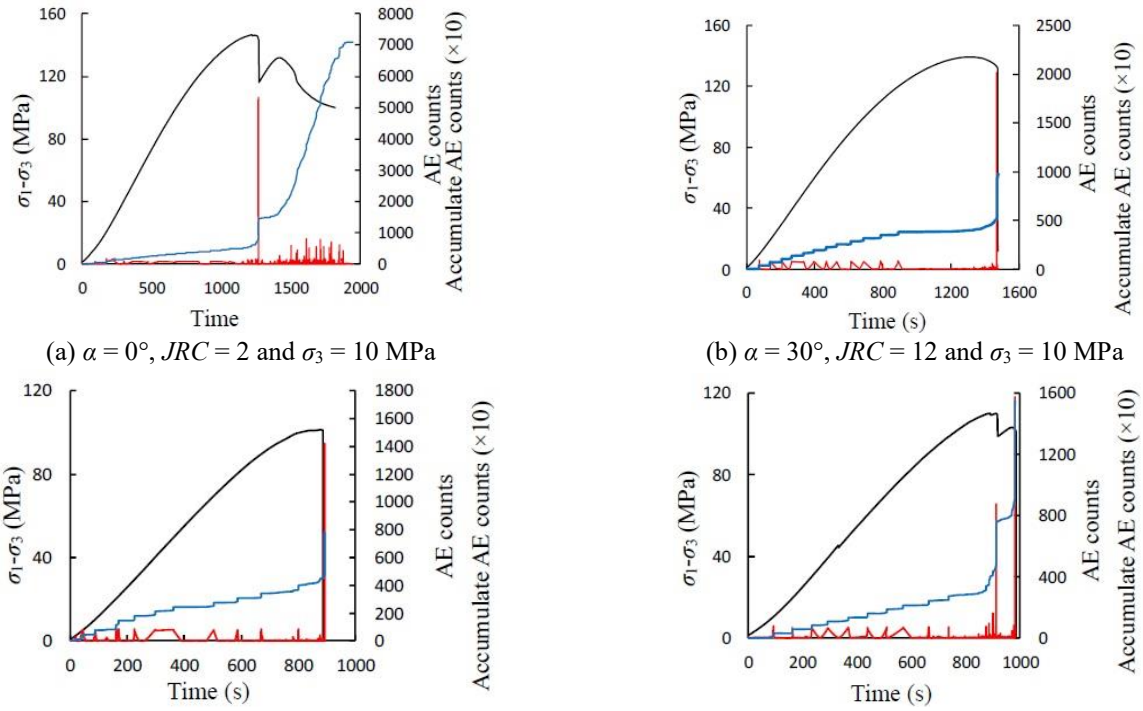

(a) α = 0°, *JRC* = 2 and σ_3 = 10 MPa

(b) α = 30°, *JRC* = 12 and σ_3 = 10 MPa

(c) α = 60°, *JRC* = 12 and σ_3 = 10 MPa

(d) α = 90°, *JRC* = 12 and σ_3 = 10 MPa

Fig. 11 Triaxial experiment stress-strain curve and acoustic emission curve of rock samples

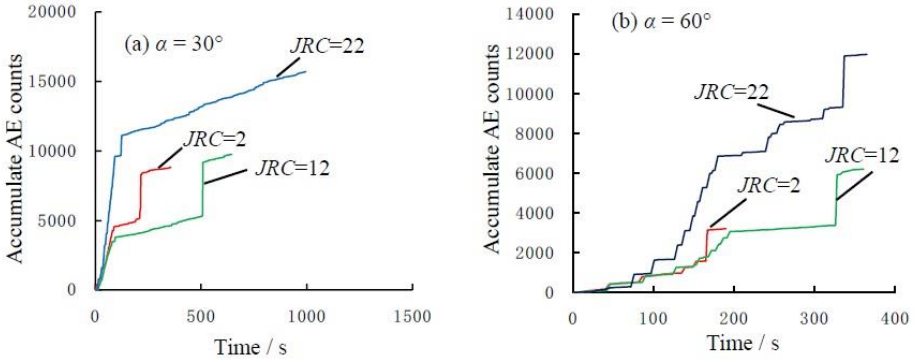

Fig. 12 AE characteristic of joint rock samples with different *JRC* when σ_3 =10MPa

axial stress continues to increase, the specimen begins to enter the yielding stage, in which the lower internal material of the specimen yields gradually and loses its bearing capacity, and the higher ones will bear higher stress until yielding failure. This shows failure development in the specimen, and micro-cracks inside the specimen initiate gradually. At this stage, AE event begin to become active, AE counts increase rapidly, and the cumulative counts of AE approaching to the peak stress is significantly larger, which marks that the specimen begin to be failed.

Once the axial stress reaches the ultimate bearing capacity of the specimen, it enters the failure stage. A larger AE event occurred in the specimen when macro-cracks appear in it. The AE event become extremely active: the AE count is rapidly increased and the AE count reaches to the maximum as soon as the specimen is failed. After the peak strength, AE of joint specimen shows different characters. When α = 0°, *JRC* = 2 and σ_3 = 10 MPa, the specimen still has a certain bearing capacity under the confining pressure due to the friction between the joint and crack surface. And, there is less AE counts can be monitored. However, other specimens show the brittle failure characteristic, and stress drop to near zero suddenly.

Fig. 12 shows the cumulative AE counts of different *JRC* with α = 30° and 60° when σ_3 =10 MPa. It can be seen that the cumulative AE counts of specimen increases with the increase of *JRC*. Although the counts of AE events cannot be in one-to-one correspondence with the number of cracks generated, it can roughly reflect the change of cracks in number to some extent. The fact that the cumulative AE counts increases with the increase of *JRC*, which indicates that the rock failure is affected by the roughness of the joint surface. It consistent with the specimen with α = 0°, whose number of cracks on the joint surface increases with the increase of *JRC*. Therefore, the roughness of the joint surface is closely related to the failure mode of the

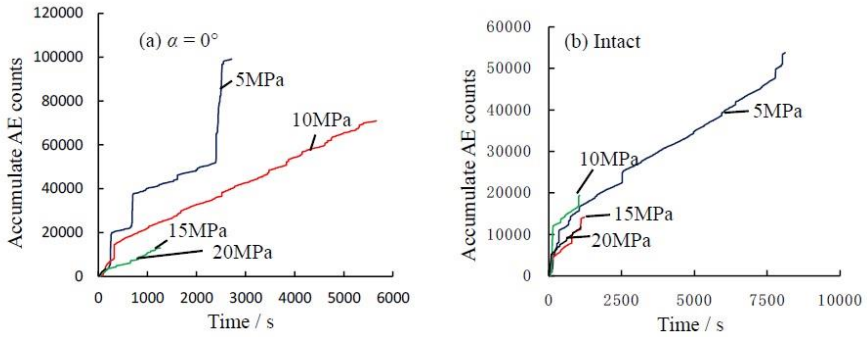

Fig. 13 AE characteristic of joint rock samples under different confining pressure

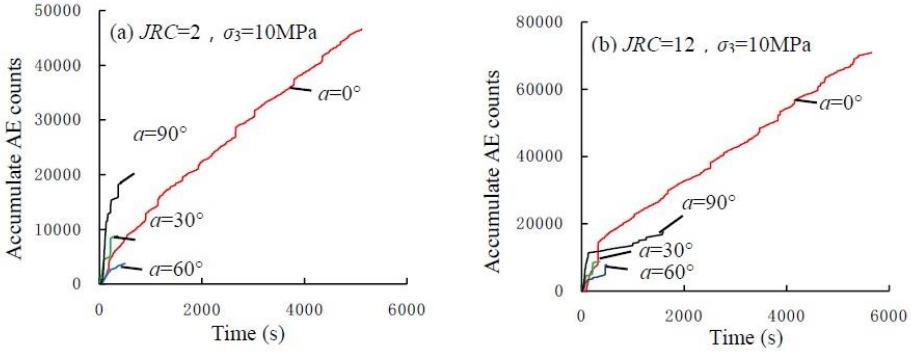

Fig. 14 AE characteristic of joint rock samples with different joint inclination angle

specimen. It can be seen that the number of crack is more sensitive to the joint surface roughness when $\alpha = 60°$.

Fig. 13 shows the cumulative AE counts for intact specimen and jointed specimen with $\alpha = 0°$ and $JRC = 12$ under different confining pressure. Obviously, the cumulative counts of AE reach the maximum when σ_3 =5 MPa. Confining pressure can inhibit the damage of specimens, so the number of cracks in the specimen will decrease as the confining pressure increases, and the cumulative counts of AE will also decrease.

Fig. 14 shows the cumulative AE counts for jointed specimens with JRC =2 and 12 under σ_3 = 10 MPa. It can be seen that the cumulative AE counts of specimens under the same JRC value decreases first and then increases with the increase of α, and it reaches the maximum at $\alpha = 0°$, while reaches the minimum at $\alpha = 60°$. It can be found that the cumulative AE counts of the specimen with $\alpha = 0°$ when σ_3 = 10 MPa exceeds the other three kinds of α. It manifests that the specimens have the largest number of cracks and the most serious damage when $\alpha = 0°$, which is consistent with the specimen failure graph. In addition, there is a little difference in number of accumulate AE counts for jointed specimens with α =30°, 60°, and 90°. When $JRC = 2$, the accumulate AE counts are 8820, 6905 and 18471, respectively; and when $JRC = 12$, the accumulate AE counts are 9761, 7814 and 17511, respectively. Although the failure modes of the specimen with $\alpha = 0°$ and 90° are all the axial splitting failure, the accumulate AE counts with $\alpha = 0°$ is significantly higher than that of $\alpha = 90°$, which indicates that the specimen with $\alpha = 90°$ is still destroyed along the joint surface. And the reason why the number of cracks of the specimen with $\alpha = 90°$ is significantly lower than that with $\alpha = 0°$ is that its failure is relatively more severe through the intact part.

5. Discussions

The mechanical behavior of jointed has become a major concern during the recovery of unconventional resources, including shale gas, enhanced geothermal system, and carbon dioxide sequestration, the injection of large volumes of fluid into the subsurface can reactivate pre-existing faults (An *et al.* 2020), which on the one hand can create crack network to enhance the production of energy, on the other hand can trigger seismicity (Elsworth *et al.* 2016). Understanding the mechanical behavior of jointed rock is vital to enhance energy production and mitigate the hazard. Considerable attention has been paid to joint roughness since the 1960s (Patton 1966), mostly focused on the strength and dilation deformation caused by direct shear tests. And, under direct shear tests, three typical failure modes observed under direct shear tests were summarized, as Type I, sliding along the rock joint (under low normal stress), Type II, shearing partly through asperities (under moderate normal stress) and Type III, mostly shearing through the rock block (under high normal stress) (Guo and Qi 2015). However, the jointed rock always under deep underground, and it subject to triaxial stress. Therefore, the triaxial compression tests can reflect the environment more veritable. From the above result obtained by triaxial compression, it indicates that the failure models are more

complex compared with that under direct shear tests. The failure not only along the joint surface, but also occur in the intact part. Based on the experimental result, three typical failure models are classified, which can provide suggestion for energy production increasing and hazard mitigation.

To analyze the compressive strength of rough joint specimens theoretically, Jaeger and Cook (1979) indicated that the theory of single structural plane can be proposed as the basis of research.

Fig. 15 presents a schematic diagram of theoretical analysis of joint surfaces, and the angle between the normal of the joint surface and the maximum principal stress is 45°. The Mohr stress circle theory and the Coulomb shear criterion of joint surface can be used to obtain the shear failure equation along the joint surface

$$\sigma_1=\sigma_3+(2c_j+\sigma_3\tan\varphi_j)/[(1-\tan\varphi_j\cot a)\sin\alpha] \quad (5)$$

where σ_1 is the maximum principal stress at failure; σ_3 is the confining pressure; c_j, φ_j are the bonding force and internal friction angle of the joint surface; α is the joint inclination. $\sigma_n = \sigma_1\cos\alpha+\sigma_3\sin\alpha$ and $\tau = \sigma_1\sin\alpha+\sigma_3\cos\alpha$, $\tau_{max} = c_j+\sigma_n\tan\varphi_j$ when the joint surface reaches the peak shear strength. The above equation shows that when the axial pressure of the specimen meets the condition, the stress on the joint surface of the specimen is in the equilibrium state.

It can be found from the Eq. (5) that σ_1 tends to be infinite when $\alpha = 90°$, so it is hard to fail along the joint. It is necessary to derive α in order to find the value of a at the minimum value of σ_1, so let the first derivative of α be zero, and the condition that σ_1 takes the minimum value is $\alpha = 45°+\varphi_j/2$.

By Moore's strength theory, Cai (2002) derived the relationship between σ_1 and α of rock mass when σ_3 is constant, where

$$\alpha_1 = \varphi_j/2+\arcsin[(\sigma_1+\sigma_3+2c_j\cot\varphi_j)\sin\varphi_j/(\sigma_1-\sigma_3)]/2 \quad (6)$$

$$\alpha_2 = 90°+\varphi_j/2-\arcsin[(\sigma_1+\sigma_3+2c_j\cot\varphi_j)\sin\varphi_j/(\sigma_1-\sigma_3)]/2 \quad (7)$$

In Fig. 16, area 1 represents the failure through intact part, area 2 shows the sliding along the joint surface, and the horizontal line intersects the joint surface failure curve at two points a, b. When $\alpha_1 < \alpha < \alpha_2$, the rock slippage along the joint surface. When $\alpha < \alpha_1$ or $\alpha > \alpha_2$, the rock mass does not break along the joint surface. At this time, the strength of the rock mass depends on the rock strength, and it has nothing to do with the existence of the joint surface. When the maximum principal stress σ_1 is perpendicular or parallel to the joint plane, the strength of the specimen is independent of the joint plane, and the strength of the specimen is determinated by material strength. When $\alpha = 45°+\varphi_j/2$, the rock mass is completely slippage along the joint surface, and the strength of the specimen is determinated by the strength of the joint surface. When the angle between σ_1 and the joint surface do not belong to the above three cases, the rock mass is destroyed not only along the joint surface, but also there will be intact part failure of it.

To understand the variation of shear stress and strength in the joint surface with JRC and confining pressure, the Barton's model (Barton and Choubey 1997) was used

$$\tau=\sigma_n\tan(JRC\log(\frac{JCS}{\sigma_n})+\varphi_b) \quad (8)$$

Where *JCS* is the joint wall compressive strength and φ_b is the basic friction angle.

In this work, *JCS* treated as the uniaxial compressive strength of intact specimen, which can be regressed, and it is 90.00 MPa. φ_b is the frictional angle of intact specimen, which can be obtained from the triaxial compressive test, and it is 42.84. The jointed specimens with $\alpha = 60°$ are selected to analyze the effect of *JRC* and confining pressure, as shown in Fig. 17. When *JRC* = 2, σ_3=15 MPa, the shear strength is larger than shear strength at initial loading stage, as shown in Fig. 16(a). However, the increasing rate of shear stress is larger than shear strength, and when axial stress exceed 13.4 MPa, the shear stress larger than the shear strength, and the specimens show the shear failure mode along the joint. When *JRC* = 22, σ_3=15 MPa, it can be seen from Fig. 17(b) that the intersection of shear stress and strength backwards, which means that the shear failure is hard than that when *JRC* = 2. Therefore, the specimen may be failure with shear cracks along with

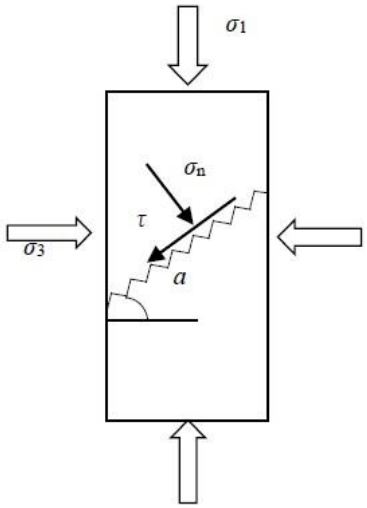

Fig. 15 Joint surface force diagram

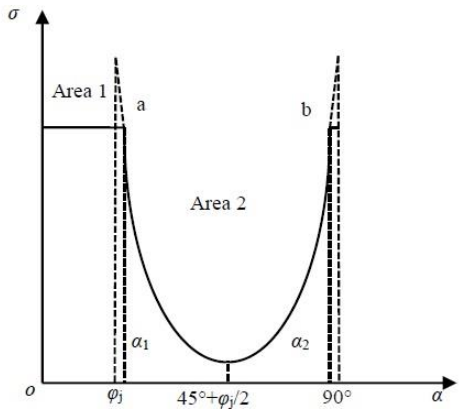

Fig. 16 Mechanics effect of joint surface (Cai 2002)

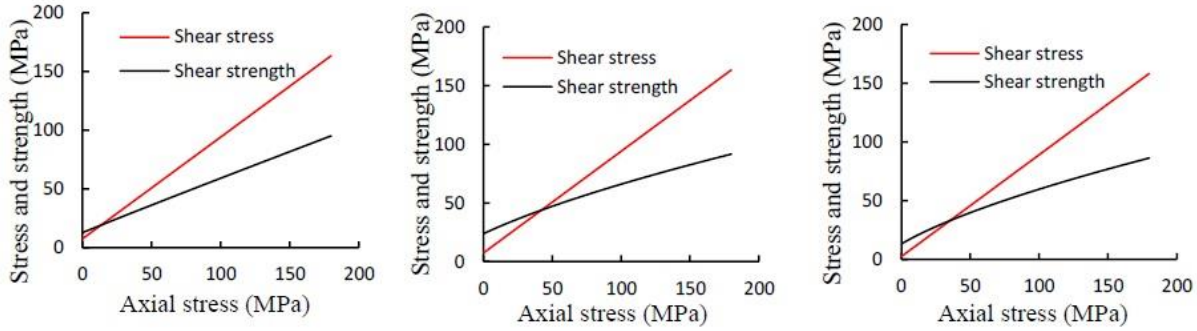

(a) JRC = 2, σ_3=15 MPa (b) JRC = 22, σ_3=15 MPa (c) JRC = 22, σ_3=5 MPa

Fig. 17 The evolution of shear stress and strength of the jointed specimens (α = 60°) with different JRC and confining pressure

(a) Axial splitting failure α = 30°, JRC = 22 and σ_3 = 5 MPa (b) Mixture failure of tension-shear α = 30°, JRC = 2 and σ_3 = 5 MPa

(c) Shear slip failure (sliding along the joint) α = 60°, JRC = 2 and σ_3 = 10 MPa (d) Shear slip (shearing clipping the asperity) α = 60°, JRC = 22 and σ_3 = 5MPa

Fig. 18 Microgram of joint dimension damage of joint rock samples

tensile cracks. With decreasing confining pressure, the intersection of shear stress and strength also forwards, as shown in Fig. 17(c), which means that confining pressure also restrain shear failure. From above analysis, it can be founded that Barton's model also can be used to predict the failure modes of jointed specimen under triaxial compression.

Under the triaxial test, the strength of the specimen increases gradually with JRC. When α = 0° and 90°, JRC has little effect on the peak strength of the rock. However, according to the joint surface crack diagram of α = 0°, it can be found that although JRC has little effect on the peak strength of the rock, it will affect the failure mode of the rock. It can be found from the Table 1 that when JRC = 2 and 12, the failure mode of the specimen with α = 30° is all the mixture failure of tension-shear, but when the JRC is increased to 22, the failure mode of the specimen becomes the single axial splitting failure. When JRC smaller, the shear and compressive strength of specimen is reach at the same time, thus the specimen failed with tensile and shear cracks. However, the shear strength increases with the increase of JRC, and the compressive strength first reached, thus the specimen failed with axial splitting tensile failure. In addition, at low confining pressure, when JRC = 22 and α = 60°, the specimen only shows shear slip failure along the joint surface, but when σ_3 increased to 15MPa or 20MPa, the specimens show mixture failure. This indicates that the confining pressure, JRC and α are mutually influential.

The KH3000 digital 3D video microscopy system is used to observe the joint surface. The specimens with α = 30°, *JRC* = 22 and σ_3 = 5 MPa; α = 30°, *JRC* = 2 and σ_3 = 5 MPa; α = 60°, *JRC* = 2 and σ_3 = 10MPa; α = 60°, *JRC* = 22 and σ_3 = 5 MPa are selected. The observation of the failure specimen shows that there are mainly three types of failure to the specimen: the first is the axial splitting, the second is the mixture of tension-shear failure and the third one is the shear slip failure, just as shown in Figs. 18(a)-18(c). The shear slip failure of the specimen mainly includes three cases: 1) shearing clipping the asperity, 2) shearing partly through asperity, 3) sliding along the joint, as shown in Figs. 18(c) and 18(d). This three cases also can be obtained by direct shear tests (Haberifield and Johnston 1994), it also can be seen in the numerical results obtained by Bahaaddini *et al.* (2016).

As shown in the Table 1, when α = 30°, the axial splitting failure only can be observed when *JRC* = 22. In addition, through the surface of jointed specimens with α = 30° and *JRC* = 22 (as shown in Fig. 18(a)), it can be seen that the asperities on the joint surface are intactness, and there is an axial splitting crack through the joint surface. It indicates that the shear strength of the joint surface is very large when α = 30° and *JRC* = 22. As the axial load increases gradually, the compressive strength of the specimen is reached, and the axial splitting failure of the specimen occurs. While when α = 30° and *JRC* = 2, there is a difference of the morphology of joint surface between that in Fig. 18(a). The joint surface has not only the axial splitting cracks but also the shear traces on asperity, as shown in Fig. 18(b). The shear stress generated by the axial pressure exceeds the shear strength of the joint surface, which make the joint surface has obvious compression-shear scratch. It shows that when *JRC* = 2, the shear strength of joint surface is not enough. Moreover, with the increase of axial load, the overall compressive strength of the specimen is also reached, causing the mixture failure of tension-shear happen. As shown in Fig. 18(c), when α = 60° and *JRC* = 2, the shear stress on the joint surface is too large. So, the shear-slip failure along the joint surface appeared and compression-shear scratch appear on the joint surface as well. As shown in Fig. 18(d), when α = 60° and *JRC* = 22, it can be found that the asperities are seriously damage, indicating that *JRC* has significant influence on the failure mode.

At low confining pressure, when the specimen reaches the yield stress, the friction provided by the confining pressure cannot suppress the slip between the joint. Therefore, the specimen is plastically strained and has an obvious shear failure surface. As the confining pressure increases and the axial stress continues to increase during the yielding of the specimen, the confining pressure and the axial stress together provide the normal stress, making the frictional bearing capacity of the joint surface increasing, and inhibit the slip of the joint surface. Therefore, swelling rather than shear slip failure was obviously observed at high confining pressure. The specimen gradually yields and the new cracks are generated, and then the plastic deformation continues to increase, causing the specimen to exhibit a yielding platform during axial compression

The influence of *JRC* on the failure of the jointed rock is actually quite complicated. Rock joint surface damage may contain several failure modes in different load environments. For example, tensile splitting occurs at a portion with a larger roughness, and shear slip occurs at a joint surface which have a smaller roughness. The roughness of joint surface in this paper only reflects a special case of joint surface damage, and the research on the roughness of joint surface needs to be further studied. Moreover, the effect of *JRC* is only for the whole specimen in this research, and the internal friction angle and cohesion at the joint surface have not been studied yet. It is necessary to carry out the direct shear test of specimens on the basis of the conventional triaxial test so that obtain the microscopic changes of *JRC* on the joint plane.

6. Conclusions

In this research, the relationship between deformation parameters, strength, failure characteristics of the jointed specimens and *JRC*, joint angle, confining pressure is analyzed by performing the triaxial compression tests of the rock–like material specimens, and following significant conclusions can be obtained.

- The peak strength of the specimen is affected not only by *JRC*, but also by α. When σ_1 is perpendicular or parallel to the joint plane, the strength of the specimen is independent of the joint plane, and the strength of the specimen is determined by material strength. When $\alpha = 45°+\varphi_j/2$, the rock mass is destroyed along the joint surface, and the strength of the specimen is determined by shear strength of the joint surface. When the angle do not belong to the above two cases, the rock mass is destroyed not only along the joint surface, but also in the intact part of specimen.
- there are three main failure types: shear slip failure, axial splitting failure and mixture failure of tension-shear, respectively. When α = 0° and 90°, the jointed specimens are predominated by axial splitting failure; while when α = 30°, the jointed specimens mainly belong to mixture failure of tension-shear; and in the case where α = 60°, most of the jointed specimens are shear slip failure along the joint plane.
- With the increase of *JRC*, the AE cumulate counts increases gradually as well. Meanwhile, the confining pressure can protect the rock to some extent, that is, with the increase of the confining pressure, the AE cumulate counts decreases gradually. In addition, AE cumulate counts first decrease and then increase with the increase of α.

Acknowledgements

This research was supported by the National Natural Science Foundation of China (42107159, 51909260) and Fundamental Research Funds for the Central Universities (2021ZDPYJQ002).

References

Abolfazli, M. and Fahimifarb, A. (2020), “An investigation on the correlation between the joint roughness coefficient (JRC) and

joint roughness parameters", *Constr. Build. Mater.*, **259**, 120415. https://doi.org/10.1016/j.conbuildmat.2020.120415.

An, M.K., Zhang, F.S., Elsworth, D., Xu, Z.Y., Chen, Z.W. and Zhang, L.Y. (2020), "Friction of longmaxi shale gouges and implications for seismicity during hydraulic fracturing", *J. Geophys. Res. Solid Earth*, **125**(8), 1-20. https://doi.org/10.1029/2020JB019885.

Bahaaddini, M., Hagan, P.C., Mitra, R. and Khosravi, M.H. (2016), "Experimental and numerical study of asperity degradation in the direct shear test", *Eng. Geol.*, **204**, 41-52. https://doi.org/10.1016/j.enggeo.2016.01.018

Ban, L.R., Du, W.S., Jin, T.W., Qi C.Z. and Li X.Z. (2021), "A roughness parameter considering joint material properties and peak shear strength model for rock joints", *Int. J. Min. Sci. Technol.*, **31**, 413-420. https://doi.org/10.1016/j.ijmst.2021.03.007.

Barton, N. (1973), "Review of a new shear-strength criterion for rock joints", *Eng. Geol.*, **7**(4), 287-332. https://doi.org/10.1016/0013-7952(73)90013-6.

Barton, N., Choubey, V. (1977), "The shear strength of rock joints in theory and practice", Rock Mechanics, **10**(1-2), 1-54. https://doi.org/10.1007/BF01261801

Cai, M., Hou, P.Y., Zhang X.W. and Feng X.T. (2021), "Post-peak Stress–Strain curves of brittle hard rocks under axial-strain-controlled loading", *Int. J. Rock Mech. Min. Sci.*, **14**, 104921. https://doi.org/10.1016/j.ijrmms.2021.104921

Cai, M.F. (2002), "Rock mechanics rock engineering", **8**, 21-21.

Diamantis, K. (2019), "Estimation of tensile strength of ultramafic rocks using indirect approaches", *Geomech. Eng.*, **17**(3), 261-270. https://doi.org/10.12989/gae.2019.17.3.261.

Elsworth, D., Spiers, C.J. and Niemeijer, A.R. (2016), "Understanding induced seismicity", *Science*, **354**(6318), 1380-1381. https://doi.org/10.1126/science.aal2584

Grasselli, G. (2006), "Manuel rocha medal recipient shear strength of rock joints based on quantified surface description", *Rock Mech. Rock Eng.*, **39**(4), 295. https://doi.org/10.1007/s00603-006-0100-0.

Grasselli, G., Wirth, J. and Egger, P. (2002), "Quantitative three-dimensional description of a rough surface and parameter evolution with shearing", *Int. J. Rock Mech. Min. Sci.*, **39**(6), 789-800. https://doi.org/10.1016/S1365-1609(02)00070-9.

Grasselli, G. and Egger, P., (2003), "Constitutive law for the shear strength of rock joints based on three-dimensional surface parameters", *Int. J. Rock Mech. Min. Sci.*, **40**(1), 25-40. https://doi.org/10.1016/S1365-1609(02)00101-6.

Guo, S.F. and Qi, S.W. (2015), "Numerical study on progressive failure of hard specimens with an unfilled undulated joint", *Eng. Geol.*, **193**, 173-182. https://doi.org/10.1016/j.enggeo.2015.04.023.

Haberifield, C. and Johnston, I. (1994), "A mechanistically-based model for rough rock joints", *Int. J. Rock Mech. Min. Sci.*, **39**, 731-741. https://doi.org/10.1016/0148-9062(94)90898-2.

He, L., Zhao, Z., Chen, J. and Liu, D. (2020), "Empirical shear strength criterion for rock joints based on joint surface degradation characteristics during shearing", *Rock Mech. Rock Eng.*, **53**, 3609-3624. https://doi.org/10.1007/s00603-020-02120-4.

Hojat, N., Saeed, K.N. and Hossein, J. (2021), "Geostatistical algorithm for evaluation of primary and secondary roughness", *Geomech. Eng.*, **24**, 359-370. https://doi.org/10.12989/gae.2021.24.4.359.

Jaeger, J.C. and Cook N. (1979), "Fundamentals of rock mechanics. Third edition", *Science Paperbacks*, **9**(3), 251-**252**(2). https://doi.org/10.1111/j.1468-8123.2009.00251.x.

Jafari, M.K., Hosseini, K.A., Pellet, F., Boulon, M. and Buzzi, O. (2003), "Evaluation of shear strength of rock joints subjected to cyclic loading", *Soil Dynam. Earthq. Eng.*, **23**(7), 619-630. https://doi.org/10.1016/S0267-7261(03)00063-0.

Lee, H., Oh, T.M. and Park, C., (2020), "Analysis of permeability in rock fracture with effective stress at deep depth", *Geomech. Eng.*, **22**(5), 375-384. https://doi.org/10.12989/gae.2020.22.5.375.

Mamen, B. and Hammoud, F. (2021), "Microstructural observations of shear zones at cohesive soil-steel interfaces under large shear displacements", *Geomech. Eng.*, **25**(4), 275-281. https://doi.org/10.12989/gae.2021.25.4.275.

Marsch, K. and Fernandez-Steeger, T.M. (2021), "Comparative evaluation of statistical and fractal approaches for jrc calculation based on a large dataset of natural rock traces", *Rock Mech. Rock Eng.*, **54**, 1897–1917. https://doi.org/10.1007/s00603-020-02348-0

Park J.W. and Song J.J. (2013), "Numerical method for the determination of contact areas of a rock joint under normal and shear loads", *Int. J. Rock Mech. Min. Sci.*, **58**, 8-22. https://doi.org/10.1016/j.ijrmms.2012.10.001.

Patton, F.D. (1966), "Multiple modes of shear failure in rock", *Proceeding of the Congress of International Society of Rock Mechanics*, 509-513.

Renaud, S., Tarik, S., Bouaanani, N., Miquel, B., Quirion, M. and Rivard, P. (2019), "Roughness effects on the shear strength of concrete and rock joints in dams based on experimental data", *Rock Mech. Rock Eng.*, **52**, 3867-3888. https://doi.org/10.1007/s00603-019-01803-x.

Samanta, M., Punetha, P. and Sharma, M. (2018), "Effect of roughness on interface shear behavior of sand with steel and concrete surface", *Geomech. Eng.*, **14**(4), 387-398. https://doi.org/10.12989/gae.2018.14.4.387.

Saadat, M. and Taheri, A. (2020) "A cohesive grain based model to simulate shear behaviour of rock joints with asperity damage in polycrystalline rock", *Comput. Geotech.*, **117**, 103254. https://doi.org/10.1016/j.compgeo.2019.103254.

Singh, H.K. and Basu, A. (2016), "Shear behaviors of 'real' natural un-matching joints of granite with equivalent joint roughness coefficients", *Eng. Geol.*, **211**, 120-134. https://doi.org/10.1016/j.enggeo.2016.07.004.

Wang, Z., Gu, L.L., Shen, M.R., Zhang F., Zhang G.K. and Wang X. (2019), "Shear stress relaxation behavior of rock discontinuities with different joint roughness coefficient and stress histories", *J. Struct, Geol.*, **126**, 272–285. https://doi.org/10.1016/j.jsg.2019.06.016

Xia, C.C., Song, Y.L., Tang, Z.C. and Song Y.J. (2012), "Shear strength and morphology characteristic evolution of joint surface under cyclic loads", *J. Central South Univ.*, **43**(9), 3589-3594.

Xie, H.P., Wang, J.A. and Stein, E. (1998), "Direct fractal measurement and multifractal properties of fracture surfaces", *Phys. Lett. A*, **242**(1-2), 41-50. https://doi.org/10.1016/S0375-9601(98)00098-X.

Yang, S.Q., Lu, J.W., Tian, W.L., Tang, J.Z., (2018), "Experimental study of mechanical behavior of rock specimens with different joint roughness coefficient under conventional triaxial compression", *Rock Soil Mech.*, **39**, 21-32.

Yang, S.Q., Ranjith, P.G., Jing, H.W., Tian, W.L. and Ju, Y. (2017), "An experimental investigation on thermal damage and failure mechanical behavior of granite after exposure to different high temperature treatments". *Geothermics*, **65**, 180-197. https://doi.org/10.1016/j.geothermics.2016.09.008.

Yang, W.D., Wang, L., Guo J.J. and Chen, X.G. (2020), "An experimental study on shear mechanical properties of clay-concrete interface with different roughness of contact surface", *Geomech. Eng.*, **23**, 39-50. https://doi.org/10.12989/gae.2020.23.1.039.

Zandarin, M.T., Alonso, E. and Olivella, S. (2013), "A constitutive law for rock joints considering the effects of suction and

roughness on strength parameters", *Int. J. Rock Mech. Min. Sci.*, **60**(2), 333-344. https://doi.org/10.1016/j.ijrmms.2012.12.007.
Zhao, Z.H., Dou, Z.H., Xu, H.R. and Liu, Z.N. (2019), "Shear behavior of Beishan granite fractures after thermal treatment", *Eng. Fract. Mech.*, **213**, 223-240. https://doi.org/10.1016/j.engfracmech.2019.04.012.

GC